



Statistical analysis of deformation of a shock wave propagating in a local turbulent region

Cite as: Phys. Fluids **32**, 096107 (2020); <https://doi.org/10.1063/5.0019784>

Submitted: 25 June 2020 . Accepted: 24 August 2020 . Published Online: 15 September 2020

K. Tanaka (田中健人), T. Watanabe (渡邊智昭) , and K. Nagata (長田孝二) 

COLLECTIONS

 This paper was selected as an Editor's Pick



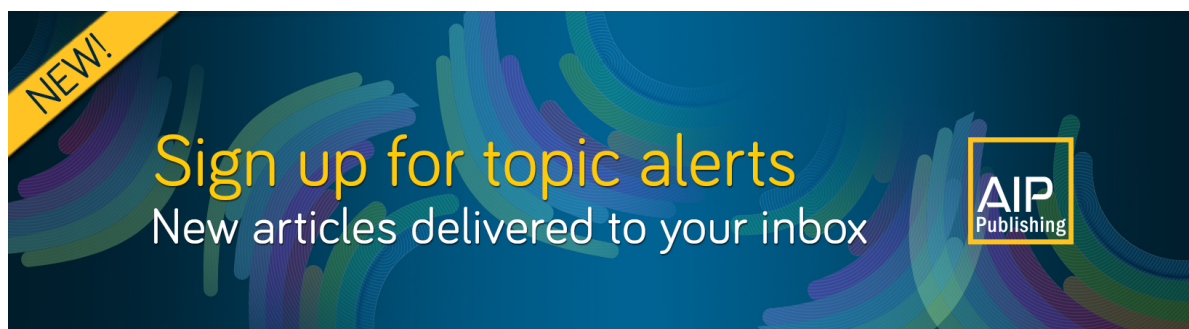
[View Online](#)



[Export Citation](#)



[CrossMark](#)





Statistical analysis of deformation of a shock wave propagating in a local turbulent region

Cite as: Phys. Fluids 32, 096107 (2020); doi: 10.1063/5.0019784

Submitted: 25 June 2020 • Accepted: 24 August 2020 •

Published Online: 15 September 2020



K. Tanaka (田中健人), T. Watanabe (渡邊智昭),^{a)}  and K. Nagata (長田孝二) 

AFFILIATIONS

Department of Aerospace Engineering, Nagoya University, Furo-cho, Chikusa, Nagoya 464-8603, Japan

^{a)} Author to whom correspondence should be addressed: watanabe.tomoaki@c.nagoya-u.jp

ABSTRACT

Direct numerical simulation is performed for analyzing the interaction between a normal shock wave and turbulence. The shock wave is initially located in a quiescent fluid and propagates into a local turbulent region. This flow setup allows investigation of the initial transition and statistically steady stages of the interaction. Shock deformation is quantified using the local shock wave position. The root-mean-square (rms) fluctuation in the shock wave position increases during the initial stage of the interaction, for which the time interval divided by the integral time scale increases with $M_t^2/(M_s^2 - 1)$, where M_t is a turbulent Mach number and M_s is a shock Mach number. In late time, the rms fluctuation in the shock wave position hardly depends on the propagation time and follows a power law, $[M_t^2/(M_s^2 - 1)]^{0.46}$, whose exponent is similar to the power law exponent of the rms pressure-jump fluctuation reported in experimental studies. Fluctuations in the shock wave position have a Gaussian probability density function. The spectral analysis confirms that the length scale that characterizes shock wave deformation is the integral length scale of turbulence. The fluctuating shock wave position is correlated with dilatation of the shock wave, where the correlation coefficient increases with $M_t/(M_s - 1)$. In addition, the shock wave that deforms backward tends to be stronger than average and vice versa. Mean pressure jumps across the shock wave are different between areas with forward and backward deformations. This difference increases with the rms fluctuation in the shock wave position and is well-represented as a function of $M_t^2/(M_s^2 - 1)$.

Published under license by AIP Publishing. <https://doi.org/10.1063/5.0019784>

I. INTRODUCTION

The interaction between shock waves and turbulence is an important phenomenon in various fields such as physics and engineering. Shock waves are generated by, for example, supernova explosion,¹ inertial confinement fusion,² and supersonic aircraft flights.³ Propagation of shock waves in turbulence affects the characteristics of the shock wave and turbulence. The shock waves generated by supersonic aircraft flights are observed as big noise, called a sonic boom, which threatens our living environment and living ecosystem. Sonic booms possibly influence the attitude and behavior of animals, although physical damage to them is unlikely; however, the boom can break glass windows and crack the plaster of buildings even though it does not cause significant damage to building structures.⁴ Therefore, sonic booms are one of the biggest problems facing the realization of future supersonic transportation. In the flight test of a supersonic airplane, pressure waveforms of the sonic boom

were measured at various observation points on the ground.³ These waveforms were different at each observation point. The interaction of a shock wave with atmospheric turbulence causes variation in the pressure waveform; therefore, the effects of the interaction need to be incorporated in sonic boom prediction, as reported in recent studies.⁵

Previous numerical and experimental studies have investigated the shock wave–turbulence interaction. Direct numerical simulation (DNS) of a normal shock wave propagating in homogeneous isotropic turbulence has been widely used for investigating the statistical properties of turbulence after the interaction.^{6–11} The shock wave–turbulence interaction amplifies the turbulent kinetic energy and enstrophy. In addition, characteristic length scales of turbulence are affected by the interaction because of strong compression in the shock normal direction. Similar effects on turbulence have been confirmed in experiments involving a normal or spherical shock wave propagating in grid turbulence.^{12–14} These changes in

turbulence statistics have also been studied theoretically using the linear interaction analysis, rapid distortion theory, and quasi-equilibrium assumption.^{10,15–23}

Shock waves are strongly affected by turbulence. DNS studies have reported that the geometry of the shock surface changes upon interaction with turbulence, whereby the shock wave can be wrinkled or locally broken by the interaction.^{10,24,25} Shock surface deformation was also experimentally observed in a shadowgraph visualization of a shock wave interacting with grid turbulence produced in a shock tube.²⁶ No discontinuous jumps of physical variables exist in the broken area of the shock wave. The shock surface geometry, e.g., appearance of broken regions, is often characterized by functions of the shock Mach number $M_s = U_s/a$ and the turbulent Mach number $M_t = \sqrt{3}u'_{rms}/a$, where a is the speed of sound in front of the shock wave, U_s is the shock propagation speed, and u'_{rms} is the root-mean-square (rms) velocity fluctuation in turbulence.^{24,25} DNS of a normal shock wave showed that the interaction induces fluctuations in density and pressure jumps across the shock wave.^{10,27} Experiments involving spherical shock waves interacting with turbulence also confirmed fluctuations in the pressure jumps of the shock waves.^{28–33} These jumps are directly related to the shock Mach number by the Rankine–Hugoniot relations, and the shock strength locally fluctuates due to the interaction. Experiments involving weak shock waves showed that the rms fluctuation in pressure jumps is also well-expressed as a single function of M_s and M_t .³¹ Both numerical simulations and experiments have shown that fluctuations in pressure jumps are correlated with velocity fluctuations in the normal direction of the shock wave.^{27,30,33}

The importance of shock surface deformation due to velocity fluctuations has been recognized since theoretical works by Ribner.^{15,16} A convex part of the deformed shock wave (here, convex in the direction of propagation) is locally weakened by a so-called defocusing effect, whereas a concave shape amplifies the shock wave.³⁴ These relations between the shock surface geometry and the shock Mach number were confirmed in experiments involving a spherical shock wave and a turbulent jet, wherein shock surface deformation and shock wave strength were assessed by shadowgraph visualization and overpressure measurement.²⁸ Numerical simulations also revealed that the density jump across the shock wave is correlated with the shock wave position in relation to the mean position, which can be related to the concave or convex shape of the shock wave.²⁵ A shock deformation model that assumes deformation of a normal shock wave due to a non-uniform velocity profile^{30,32} efficiently explains the experimental and numerical findings of the correlation between the pressure jump of the shock wave and velocity of turbulence,^{27,30,33} gradual emergence of turbulent effects on the shock wave,^{27,30} and M_s and M_t dependence of the rms fluctuation in the pressure jump.³¹ The deformation of the shock wave has also been studied in the interaction between the shock wave and a single vortex.^{35–37} These previous studies on the shock wave–turbulence interaction indicate that shock wave deformation plays an important role in the physical mechanics of the shock wave modulation caused by turbulence.

Most previous studies have considered the interaction between shock waves and homogeneous turbulence because the assumption

of statistical homogeneity leads to a simple statistical description of turbulence. Once a shock wave propagates in turbulence for a long period, the shock wave characteristics become independent of the propagation time. Previous studies have mostly focused on the statistically steady state of shock waves. Experiments and numerical simulations have shown that shock surface deformation increases with time and that fluctuations in the pressure jump increase as the shock wave propagates until the statistically steady state is achieved.^{26,27,33} For better understanding of the shock wave–turbulence interaction, investigation of the initial transition stage of shock propagation in turbulence is necessary. This transition stage can be important in practical problems. For example, shock waves in sonic boom problems are influenced by atmospheric turbulent boundary layers, which possess external intermittency,³⁸ and these shock waves propagate from an outer laminar (or weakly turbulent) flow to the turbulent boundary layer.

In this paper, DNS is performed for a normal shock wave propagating toward a turbulent front from a quiescent fluid. Here, the turbulent flow is localized in space, and the shock wave–turbulence interaction occurs once the shock wave reaches the turbulent front. This turbulent flow field is generated by inserting isotropic turbulence in the middle of the quiescent fluid. The present flow setup enables us to investigate the initial transition stage of the interaction as the shock wave propagates from the quiescent fluid to the turbulence; this is unlike most previous DNS studies that focused on the statistically steady state of the interaction. Shock wave deformation induced by the interaction is studied in both the initial transition and statistically steady stages of the interaction. Shock wave deformation is quantified using local shock wave positions, which provide more detailed properties of the deformed shock wave than simple visualization of the shock surface. This study focuses on the normal shock wave and isotropic turbulence since they are the most fundamental. It should be noted that the mean velocity is zero in the turbulence in the present DNS; however, the mean velocity gradient affects the mean shock Mach number.^{33,39} This effect of an inhomogeneous mean velocity does not exist in the interaction between a shock wave and isotropic turbulence. The present analysis mostly relies on the statistics of turbulence and the shock wave. Although the statistical approach is useful in understanding phenomena related to turbulence, the statistics of turbulence sometimes veil important characteristics of the instantaneous flow field. For example, the statistical approach cannot reveal the flow structures of turbulence,⁴⁰ which are often identified by spatiotemporal distributions of physical variables, such as enstrophy and swirling strength, used to identify vortical structures.^{41–45} This study investigates the statistical properties of the shock wave–turbulence interaction in a systematic manner by presenting the results as functions of important parameters, i.e., the turbulent Mach number and shock Mach number. Section II describes details of the numerical simulations, such as numerical schemes, initial and boundary conditions, and physical and numerical parameters. The results of the numerical simulations are presented in Sec. III, and the paper is summarized in Sec. IV. Nomenclature presents the list of main symbols, while all symbols are also defined in the text when they appear.

II. DNS OF A NORMAL SHOCK WAVE PROPAGATING IN A LOCAL TURBULENT REGION

A. A normal shock wave propagating in a local turbulent region

Figure 1 shows an overview of the DNS of a shock wave that propagates from a quiescent fluid to a turbulent region. In the initial state, the normal shock wave is located in the region at rest, whereas the turbulent flow region is localized in the middle of the computational domain. The flow is periodic in the y and z directions. The shock propagation direction is denoted by x . Both sides of the turbulent region have interfaces that separate the turbulence from the quiescent fluid. The flow setup of the local turbulent region is the same as the one considered in previous studies for the turbulent/non-turbulent interface.^{46–48} The shock wave propagates toward the turbulent front and enters the turbulent region, where the shock–turbulence interaction occurs. In the DNS, time is advanced until the shock wave reaches the far side of the local turbulent region. This setup allows us to investigate the initial transition stage of the shock wave–turbulence interaction. The DNS methodology and subsequent analysis are summarized below.

1. Run a DNS of isotropic turbulence with a linear forcing scheme and store the instantaneous flow field at various time steps.
2. Run a numerical simulation of the shock wave propagating in a quiescent fluid and store the flow variables around the shock wave.
3. Generate the initial condition for the DNS of the shock–turbulence interaction from the simulations in steps 1 and 2.
4. Run the DNS of the shock–turbulence interaction. This DNS is repeated for different realizations of isotropic turbulence using the instantaneous flow field at different time steps in step 3.
5. The instantaneous flow fields saved in the DNS of the shock–turbulence interaction are analyzed statistically.

Steps 1 and 2 are explained in Secs. II C and II D, respectively. The flow considered in step 4 is described below, whereas the detailed numerical method is presented in Sec. II B. The method to calculate the statistics of the shock–turbulence interaction is presented in Sec. III.

The governing equations used in the DNS are three-dimensional, compressible Navier–Stokes equations for a perfect gas (air) and are given as follows:

TABLE I. Parameters of the simulations of the shock–turbulence interaction.

Case	M_s	M_t	$M_t/(M_s - 1)$	$M_t^2/(M_s^2 - 1)$	Re_λ	L/L_0	λ/L_0	η/L_0
1	1.3	0.13	4.2×10^{-1}	2.3×10^{-2}	64	0.56	0.18	0.011
2	1.3	0.063	2.1×10^{-1}	5.7×10^{-3}	71	0.70	0.19	0.012
3	1.3	0.011	3.7×10^{-2}	1.8×10^{-4}	59	0.74	0.17	0.012
4	1.1	0.011	1.1×10^{-1}	6.0×10^{-4}	59	0.74	0.17	0.012
5	1.01	0.011	1.1×10^0	6.2×10^{-3}	59	0.74	0.17	0.012

$$\frac{\partial \rho}{\partial t} + \frac{\partial \rho u_j}{\partial x_j} = 0, \quad (1)$$

$$\frac{\partial \rho u_i}{\partial t} + \frac{\partial (\rho u_i u_j + \delta_{ij} P)}{\partial x_j} = \frac{\partial \tau_{ij}}{\partial x_j}, \quad (2)$$

$$\frac{\partial e}{\partial t} + \frac{\partial (e + P) u_j}{\partial x_j} = \frac{\partial \tau_{ij} u_i}{\partial x_j} + \frac{\partial}{\partial x_j} \left(\kappa \frac{\partial T}{\partial x_j} \right), \quad (3)$$

$$\tau_{ij} = \mu \left(\frac{\partial u_i}{\partial x_j} + \frac{\partial u_j}{\partial x_i} - \frac{2}{3} \delta_{ij} \frac{\partial u_k}{\partial x_k} \right), \quad (4)$$

with the equation of state $P = \rho RT$, where t is the time, x_i is the position, ρ is the density, u_i is the velocity vector, $e = P/(\gamma - 1) + \rho u_i^2/2$ is the total energy, T is the temperature, P is the pressure, μ is the viscosity coefficient calculated according to Sutherland's law, κ is the thermal conductivity, $R = 287 \text{ J/(kg K)}$ is the gas constant, $\gamma = 1.4$ is the specific heat ratio, δ_{ij} is the Kronecker delta, and τ_{ij} is the shear stress tensor, expressed as Eq. (4). Hereafter, the velocity components in the x , y , and z directions are denoted by u , v , and w , respectively. The Prandtl number is $Pr = 0.71$. The size of the computational domain is $(L_x, L_y, L_z) = (32L_0, 4L_0, 4L_0)$, where the reference length scale L_0 is related to the integral length scale of turbulence, which is defined in additional simulations to generate the local turbulent region, as described in Sec. II C. The turbulence is located between $2.5L_0 \leq x \leq 22.5L_0$, whereas the initial shock wave is located at $x = 1.5L_0$. The number of computational grid points is $(N_x, N_y, N_z) = (2048, 256, 256)$ in all simulations of the shock–turbulence interaction.

Table I summarizes the simulation conditions and the characteristics of turbulence defined with volume averages in the turbulent region. The table presents the turbulent Reynolds number

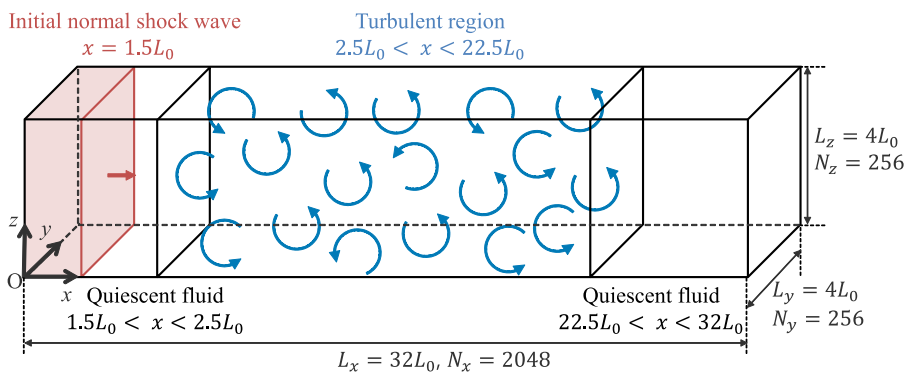


FIG. 1. Schematic of numerical simulations of a shock wave propagating from a quiescent fluid into a turbulent region.

$Re_\lambda = u'_{rms}\lambda/\langle\nu\rangle$, the integral length scale $L = \int_0^\infty f(r)dr$ calculated using the longitudinal correlation function $f(r)$, which is defined by velocity fluctuations, the Taylor microscale $\lambda = u'_{rms}/(\partial u/\partial x)'_{rms}$, and the Kolmogorov length scale $\eta = (\langle\nu\rangle^3/\langle\epsilon\rangle)^{1/4}$, where $\nu = \mu/\rho$ is the kinematic viscosity and $\epsilon = \tau_{ij}S_{ij}$ with $S_{ij} = (\partial u_i/\partial x_j + \partial u_j/\partial x_i)/2$ is the dissipation rate of the turbulent kinetic energy. These statistics are considered for isotropic turbulence, and the quiescent fluid surrounding the turbulence, as shown in Fig. 1, is not used as a statistical sample. $\langle f \rangle$ denotes a mean value of a variable f , and its rms fluctuation is denoted by f'_{rms} . The DNS is performed for five cases with different sets of the shock Mach number M_s and turbulent Mach number M_t . The computational grid size Δ is $0.016L_0$, which is equivalent to 1.4η . Grid spacing is uniform in the entire computational domain. DNS studies on turbulence have used computational grids of similar sizes extensively.^{49–52} A widely used criterion for evaluating the spatial resolution of DNS using a spectral method is $\Delta/\eta \leq 2.1$.³⁸ A resolution better than $\Delta/\eta = 2.1$ is used in the DNS as the DNS code based on the finite volume method does not have spectral resolution. Cases 1–3 are conducted for $M_s = 1.3$, whereas $M_t = 0.13, 0.063$, and 0.011 are used for investigating turbulent Mach number dependence. Cases 3–5 assume $M_t = 0.011$ for $M_s = 1.01, 1.1$, and 1.3 , for which the effects of the shock Mach number are investigated. A previous DNS outcome posited that the shock wave can be broken by the interaction with turbulence.^{10,24,25} However, in all the simulations performed in this study, the shock wave retained its surface without having any broken parts. Therefore, we investigated shock wave deformation based on the shock wave position, as explained below. In Sec. III, statistics of the shock wave are often presented against $M_t/(M_s - 1)$ and $M_t^2/(M_s^2 - 1)$, whose values are also given in Table I. All simulations are conducted for the turbulent Reynolds number Re_λ in the range of 60–70, and the Re_λ dependence of the results is weak compared with the dependence on M_s and M_t .

The local turbulent region is generated using isotropic turbulence obtained via additional DNS, as explained in Sec. II C. For each condition, the simulations of the shock–turbulence interaction are repeated five times using instantaneous flow data of the isotropic turbulence at different time steps. Furthermore, additional five simulations are performed only for case 1 in order to check statistical convergence. The statistics in case 1 are calculated using ten simulations. For assessing statistical errors, this paper presents results from two independent sets of five simulations for case 1 along with those from the ten simulations. The degree of the statistical convergence is similar in all cases as the computational domain size is the same in all simulations. Therefore, we estimate the statistical errors in cases 2–5 from case 1 by assuming that the fractional error is the same in all cases. Here, the fractional error in case 1 is defined as the difference in statistics between the five and ten simulations. The estimated errors are shown with error bars in figures in Sec. III. As shown in Sec. III, the error due to statistical convergence is minor and does not affect the discussion of the paper. We also conducted simulations with a lower turbulent Reynolds number using a single snapshot of turbulence, wherein the effects of the spatial resolution are evaluated for the statistics of the shock wave position. These issues about statistical convergence and the spatial resolution are discussed in the Appendix.

The characteristics of turbulence in Table I are obtained by ensemble averages of the snapshots used as the initial condition of

the shock–turbulence interaction. In the simulations of the shock–turbulence interaction, the flow is statistically homogeneous in the y and z directions. Statistics are calculated with averages taken on the y – z planes in each simulation and using the ensemble averages of the simulations; the resulting statistics are expressed as functions of time and x . An overbar $\bar{}$ is used for representing these averages.

B. Numerical methods

This study uses a message passing interface (MPI)-parallelized version of the in-house DNS code (Fortran 90) used in our previous study,²⁷ wherein DNS was performed for the interaction between a normal shock wave and homogeneous isotropic turbulence. The amplification of turbulent velocity fluctuations in the DNS agrees well with the theoretical prediction based on the linear interaction analysis.²⁷ Furthermore, rms fluctuations in the pressure jump of the shock wave obtained through this DNS code are consistent with the outcome of experiments conducted on the shock–turbulence interaction.³¹ The DNS code was validated by these comparisons reported in previous studies. In Sec. III B, the code is further validated by comparing the mean shock wave propagation velocity with a theoretical relation. We perform numerical simulations of the shock–turbulence interaction using a high-performance computing system in Nagoya University, whereas DNS of the isotropic turbulence described below is performed using the Earth Simulator in the Japan Agency for Marine–Earth Science and Technology. The code is based on the finite volume method with a shock-capturing scheme. Spatial discretization of inviscid terms is based on Roe flux difference splitting with a fifth-order weighted essentially non-oscillatory (WENO) scheme.²⁴ The other terms are calculated using a sixth-order central difference scheme. Time advancement is based on the four-stage, fourth-order Runge–Kutta method. The computational domain is divided in the y and z directions, and the subdomains elongated in the x direction are treated in each MPI process.

Numerical dissipation inherently caused by the Roe flux splitting may damp small-scale fluctuations in turbulence. Here, turbulence hardly decays with time during the simulations because the time scale of decay is much longer than that of shock wave propagation. We monitor the statistics in front of the shock wave during shock wave propagation; the effects of numerical dissipation are negligible for the statistics of turbulence during shock wave propagation. This is clearly confirmed by the velocity derivative skewness, which is very sensitive to the spatial resolution and numerical dissipation.^{53,54} If the effects of numerical dissipation on turbulence are not negligible, the velocity derivative skewness becomes small with time because the effective spatial resolution becomes worse owing to numerical dissipation. However, the skewness hardly changes with time, and the present numerical scheme does not cause artificial decay of turbulence. Although the present study uses DNS of Navier–Stokes equations with the shock-capturing scheme, the behavior of the shock wave in the present DNS is consistent with experiments on the shock wave–turbulence interaction, as discussed in Sec. III. Therefore, it can be considered that the DNS captures physical responses of the shock wave to turbulence.

Once the shock Mach number is specified as a computational parameter, physical variables of a shock wave can be calculated via

Rankine–Hugoniot relations using the shock Mach number and corresponding variables in front of the shock wave. Here, the initial flow state in front the shock wave is specified as an initial condition, which is explained in Sec. II C. Dirichlet boundary conditions are assumed for the boundary at $x = 0$, with the flow state behind the shock wave determined by Rankine–Hugoniot relations. Zero-gradient boundary conditions are assumed on the other side of the computational domain. Note that these conditions are not non-reflecting boundary conditions. Therefore, sponge zones with a second-order low-pass filter are employed near the boundaries in the x direction. The filter dumps the pressure waves toward the boundaries, thereby preventing the reflected waves from affecting the shock wave–turbulence interaction. Periodic boundary conditions are used for the y and z directions.

C. Initial conditions of turbulence

The local turbulent region is generated by performing additional DNS of compressible, homogeneous, isotropic turbulence with a linear forcing scheme,⁵⁵ which only forces solenoidal components of the velocity vector in the DNS used in this study. This DNS is initialized with a divergence-free random velocity field. The density field is uniform, and $\rho_0 = 1.17 \text{ kg/m}^3$. Mean pressure and temperature are $P_0 = 1.013 \times 10^5 \text{ Pa}$ and $T_0 = 300 \text{ K}$, respectively. The random velocity field in the physical space can be obtained by applying inverse Fourier transform to velocity vectors in the wavenumber space with a random phase. Here, the divergence-free condition is enforced in the phase space. Pressure fluctuations are calculated from velocity fluctuations by solving the Poisson equation for pressure under the divergence-free condition in the velocity field,⁵⁵ and then, temperature fluctuations are calculated using the equation of state. The velocity in the wavenumber space is assumed to have a turbulent kinetic energy spectrum $E(k)$ given in Ref. 38,

$$E(k) = C\varepsilon_0^{2/3} k^{-2/3} f_L(kL_0) f_\eta(k\eta_0), \quad (5)$$

$$f_L(kL_0) = \left(\frac{kL_0}{[(kL_0)^2 + c_L]^{1/2}} \right)^{\frac{5}{3} + p_0}, \quad (6)$$

$$f_\eta(k\eta_0) = \exp \left\{ -\beta \left([(k\eta_0)^4 + c_\eta^4]^{\frac{1}{4}} - c_\eta \right) \right\}, \quad (7)$$

where $C = 1.5$, $\beta = 5.2$, $p_0 = 2$, $c_L = 6.78$, and $c_\eta = 0.4$. Here, k is the wavenumber, ε_0 is the turbulent kinetic energy dissipation rate used as a parameter in the model spectrum, $L_0 = (\sqrt{3/2}u_0)^3/\varepsilon_0$ is related to the integral length scale, u_0 is the initial rms velocity, and $\eta_0 = \nu_0^{3/4}(\rho_0/\varepsilon_0)^{1/4}$ is the Kolmogorov scale (ν_0 : kinematic viscosity determined by T_0 and ρ_0). The parameters are calculated from the given turbulent Mach number and turbulent Reynolds number, which can be written as $M_t = \sqrt{3}u_0/\sqrt{\gamma RT_0}$ and $Re_\lambda = \sqrt{15}u_0^2(\nu_0\varepsilon_0)^{-1/2}$ in homogeneous isotropic turbulence, respectively. The integral length scale L_0 and rms velocity u_0 are used as reference length and velocity scales, respectively, in the simulations of the shock wave–turbulence interaction.

We perform DNS of isotropic turbulence using a modified version of the DNS code that was previously used for supersonic turbulent boundary layers and planar jets.^{56–58} Here, the eighth-order central difference scheme and the five-stage, fourth-order Runge–Kutta scheme are adapted for spatial and temporal discretization.

Following the study of Wang *et al.*,⁵⁹ the tenth-order low-pass filter⁶⁰ is applied to simulated variables at the end of each time step to prevent growth of unphysical fluctuations inherently arising from the central difference scheme. The computational domain size is $(4L_0)^3$, and the number of grid points is 256^3 , where the grid spacing is uniform. From the initial condition, time is advanced until the turbulence reaches a statistically steady state. The turbulent Mach number, turbulent Reynolds number, mean temperature, and mean pressure hardly change from the initial condition, whereas compressibility effects, such as density fluctuations and dilatation, emerge with time as the initial velocity field is purely solenoidal.

The local turbulent region shown in Fig. 1 is generated by the method used in Ref. 46, which inserts the isotropic turbulence in the middle of a quiescent fluid whose pressure and temperature are $1.013 \times 10^5 \text{ Pa}$ and 300 K , respectively. The length of the local turbulent region is $20L_0$. DNS of isotropic turbulence is conducted using a periodic box. Therefore, the turbulent region with a length of $20L_0$ is generated from a single snapshot of the isotropic turbulence using the periodicity. Periodic effects on the statistics related to the shock wave–turbulence interaction do not appear since ensemble averages are taken for the simulations with different snapshots of turbulence. The boundaries between the turbulence and quiescent fluid appear at $x = 2.5L_0$ and $22.5L_0$, as shown in Fig. 1. Variables $Q = \rho$, ρu_i , and e are smoothly adjusted between the two regions by applying a smoothing function given by

$$F[Q(x, y, z)] = Q_L + [Q(x, y, z) - Q_L]g_1(x)g_2(x), \quad (8)$$

$$g_1(x) = \frac{1}{2} + \frac{1}{2} \tanh\left(\frac{x - x_{t1}}{\delta_t}\right), \quad (9)$$

$$g_2(x) = \frac{1}{2} - \frac{1}{2} \tanh\left(\frac{x - x_{t2}}{\delta_t}\right), \quad (10)$$

where Q_L is a constant value of the variable in the quiescent fluid, $x_{t1} = 2.5L_0 + \delta_t/2$ and $x_{t2} = 22.5L_0 - \delta_t/2$ define the regions where the smoothing function is applied, and $\delta_t = 10\Delta$ is the thickness of the buffer regions. $g_1(x)g_2(x)$ is equal to 1 in most parts of the turbulent region and decreases to 0 at the edges of the turbulence. Therefore, the smoothing function ensures that variables vary smoothly between the turbulence and the quiescent fluid, while the turbulent region retains the original flow field obtained in the DNS of isotropic turbulence. Once the DNS of the shock wave–turbulence interaction is started, the buffer regions also evolve with time. As temporal evolution obeys the compressible Navier–Stokes equations, the mass, momentum, and energy conservations are still holed in the buffer regions.

D. Initial conditions of shock waves

In numerical simulations of the shock wave–turbulence interaction, profiles of conservative variables of the shock wave are inserted at around $x = 1.5L_0$, and the numerical solution for the shock wave is obtained by simulating the normal shock wave propagating in the quiescent fluid. Here, the computational domain size is $(L_x, L_y, L_z) = (16L_0, 4L_0, 4L_0)$, and the number of grid points is $(N_x, N_y, N_z) = (1024, 256, 256)$. Grid spacing is uniform in the simulations of the shock wave. The spatial resolution, numerical schemes,

and boundary conditions are the same as those used in DNS of the shock wave–turbulence interaction. The simulations of the shock wave are initialized with the profiles of variables $Q = \rho, \rho u_i$, and e given by

$$Q(x, y, z) = Q_F + (Q_B - Q_F) \left[\frac{1}{2} - \frac{1}{2} \tanh \left(\frac{x - x_{s0}}{\delta_s} \right) \right], \quad (11)$$

where the subscripts, F and B , represent values in front of and behind the shock wave, respectively. The flow state in front of the shock wave, Q_F , is the same as that in the quiescent fluid in the simulations of the shock wave–turbulence interaction. Then, Q_B is calculated from Q_F and M_s using Rankine–Hugoniot relations. The location of the shock wave is $x_{s0} = 1.5L_0$, and the initial thickness of the shock wave is $\delta_s = 10\Delta$.

Equation (11) represents a compression wave without discontinuity. The smoothed profile given by Eq. (11) is used as the initial condition since numerical oscillations can occur behind the shock wave if variables change discontinuously over one computational grid point. As time is advanced in the simulation, the compression wave propagates in the x direction. The gradient of the variables across the wave becomes steeper as the wave propagates, and the compression wave converges to a normal shock wave that can be treated using the numerical schemes used herein. Time is advanced until jumps of physical variables across the shock wave become independent of time. Profiles of the variables around the shock wave are taken from the simulation and are inserted at around $x = 1.5L_0$ as the initial condition of the DNS of the shock wave–turbulence interaction.

III. RESULTS AND DISCUSSION

A. Shock wave propagation in turbulence

Figure 2 visualizes velocity in the x direction on an x – y plane at five different time steps in case 1. Here, time is non-dimensionalized by $t_0 = L_0/u_0$. The shock wave is observed as a velocity jump, and it begins to deform once it enters the turbulent region. The deformation is small at the beginning of the interaction, as shown in Fig. 2(b). Large deformations can be seen in Figs. 2(c)–2(e) after the shock wave propagates in turbulence for a long period. This tendency is consistent with previous studies on the interaction between a normal shock wave and grid turbulence, wherein shock surface deformation increases as the shock wave propagates in turbulence.²⁶ Figure 3 shows the density (ρ) profile on the same x – y plane as in Fig. 2. Density sharply increases across the shock wave. Turbulence in case 1 has a turbulent Mach number of 0.13, for which compressibility effects are not negligible. Therefore, density fluctuations are large even in front of the shock wave. These density fluctuations are still weak compared with the density jump of the shock wave, and the shock wave propagates in the x direction without being broken.

Most experimental studies evaluate shock wave deformation using a shadowgraph or schlieren visualization.^{26,28,61} Shadowgraph and schlieren images contain information integrated along a light path, and it is difficult to relate the images to the local shock surface geometry. Therefore, it will be useful to present shadowgraph images of the DNS results for future experimental studies on the shock wave–turbulence interaction. Shadowgraph images can be constructed from three-dimensional instantaneous flow fields

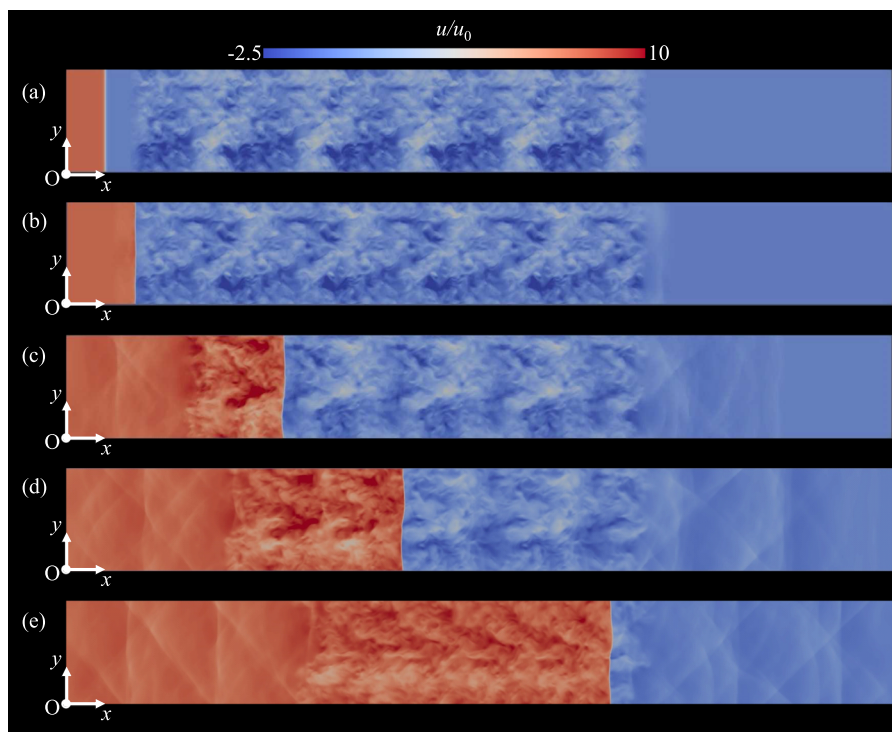


FIG. 2. Two-dimensional profiles of velocity in the x direction (u/u_0) on a x – y plane of $z = 2L_0$ at (a) $t/t_0 = 0$, (b) $t/t_0 = 0.05$, (c) $t/t_0 = 0.31$, (d) $t/t_0 = 0.52$, and (e) $t/t_0 = 0.78$.

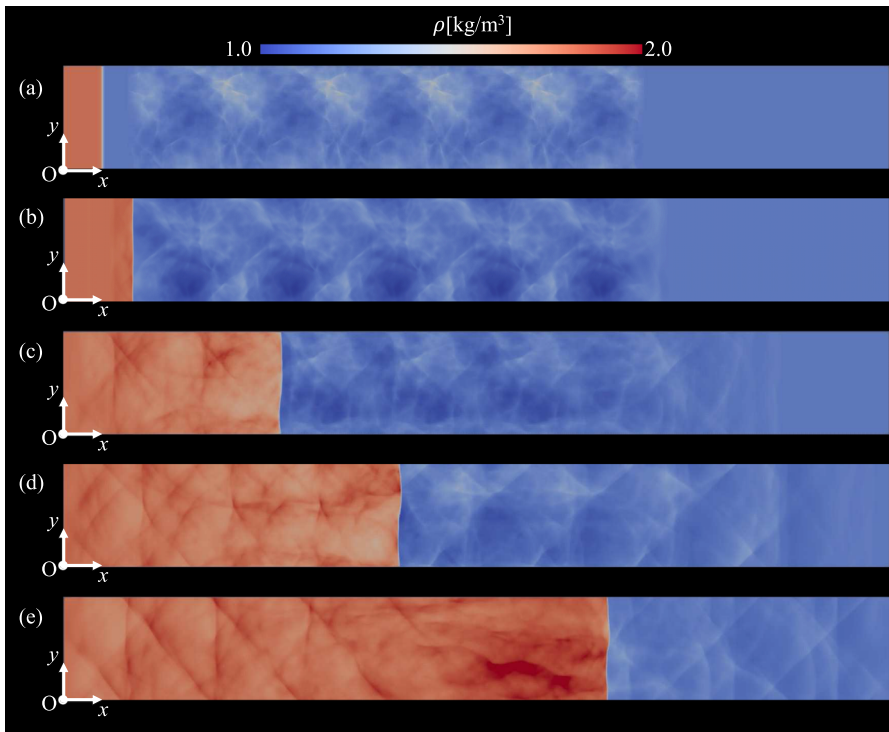


FIG. 3. Two-dimensional profiles of density on the same x - y plane as in Fig. 2 at (a) $t/t_0 = 0$, (b) $t/t_0 = 0.05$, (c) $t/t_0 = 0.31$, (d) $t/t_0 = 0.52$, and (e) $t/t_0 = 0.78$.

in DNS. The numerical shadowgraph visualization in this study assumes a paraxial hypothesis and a perfectly parallel incident light ray.⁶² Incident light with an intensity I_0 and parallel to the z direction passes through the computational domain from $z = 0$ to L_z . Diffraction of the light due to density fluctuations results in fluctuations in light intensity, $\Delta I(x, y) = I(x, y) - I_0$. Numerical shadowgraph images can be obtained by visualizing $\Delta I(x, y)/I_0$, which is calculated as

$$\frac{\Delta I}{I_0} = -l \left(\frac{\partial \varepsilon_x}{\partial x} + \frac{\partial \varepsilon_y}{\partial y} \right), \quad (12)$$

$$\varepsilon_i(x, y) = \frac{G}{n_0} \int_0^{L_z} \frac{\partial \rho}{\partial x_i} dz, \quad (13)$$

where ε_i is deviation of the light ray in the i -direction ($i = x, y$), $G = 2.3 \times 10^{-4} \text{ m}^3/\text{kg}$ is the Gladstone–Dale constant, $n_0 = 1 + \rho_0 G$ is the refractive index for air with $\rho_0 = 1.17 \text{ kg/m}^3$, and l is the distance from the end of the computational domain to a virtual screen on which the shadowgraph image is projected. Figure 4 shows the numerical shadowgraph images, in which shock waves are located at $x \approx 3.3L_0$, $9.0L_0$, or $19.0L_0$. The shock waves appear as a pair of black and white vertical lines. Comparing Figs. 4(a)–4(c), one can find that shock wave deformation increases as M_t increases from (c) to (a). This M_t dependence is consistent with previous DNS studies on the shock wave–turbulence interaction.^{24,25} The most deformed shock wave is obtained at $x \approx 19L_0$ in Fig. 4(a), where the deformed shock wave appears as multiple dark and white lines, which were also observed in experimental shadowgraph images taken for the interaction between a normal shock

wave and grid turbulence.²⁶ Turbulence, as shown in Figs. 4(c)–4(e), has $M_t = 0.011$ with different values of M_s . The shock wave is more deformed at a lower shock Mach number. Although the shock wave is largely deformed by the interaction, the shock wave in the DNS used in this study does not have any broken regions; moreover, physical variables exhibit sharp jumps in all parts of the shock wave.

B. Statistics of the local shock wave position

We investigate shock surface deformation using the local position of the shock wave $x_s(y, z; t)$. The shock wave has a large negative pressure gradient in the x direction, $\partial P/\partial x$, which is used to evaluate $x_s(y, z; t)$. Hereafter, $P_x(x)$ denotes the profile of $P_x \equiv \partial P/\partial x$ along the x direction for each (y, z) position. The shock wave position x_s is defined as the location where $P_x(x)$ attains its largest negative value. Practically, a second-order Lagrange interpolation is applied to $\partial P/\partial x$ around the computational grid point at which $\partial P/\partial x$ takes the largest negative value. A continuous profile of $P_x(x)$ is obtained via the interpolation and is used to identify x_s , which is obtained as a function of y, z , and t by repeatedly applying this procedure for all (y, z) positions in each instantaneous flow field. The present definition of the shock wave position is related to that with the dilatation $\nabla \cdot \mathbf{u}$ used in previous studies.^{24,25} Both quantities are expected to yield almost identical shock wave positions because they have similar profiles near the shock wave. Statistics of $x_s(y, z; t)$ are calculated as functions of t by taking averages in the y and z directions as well as ensemble averages of the simulations.

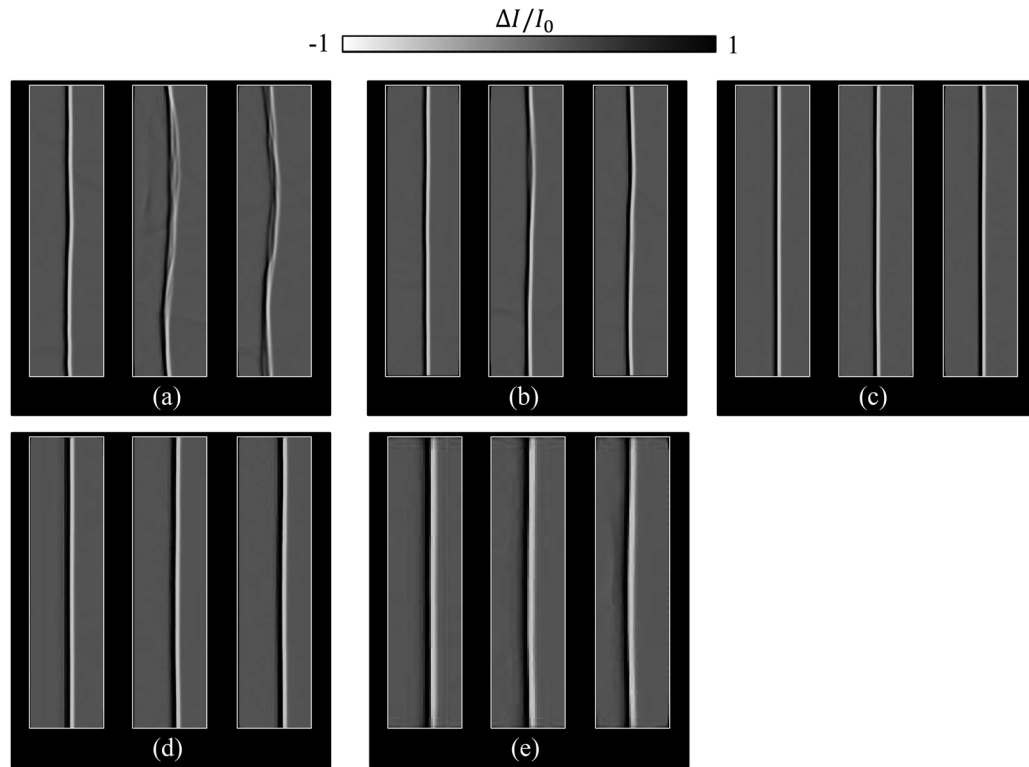


FIG. 4. Numerical shadowgraph images for the shock wave located at $x \approx 3.3L_0$, $x \approx 9.0L_0$, and $x \approx 19L_0$ from left to right in each figure. (a) Case 1 ($I/L_0 = 1$), (b) case 2 ($I/L_0 = 1$), (c) case 3 ($I/L_0 = 1$), (d) case 4 ($I/L_0 = 5$), and (e) case 5 ($I/L_0 = 100$).

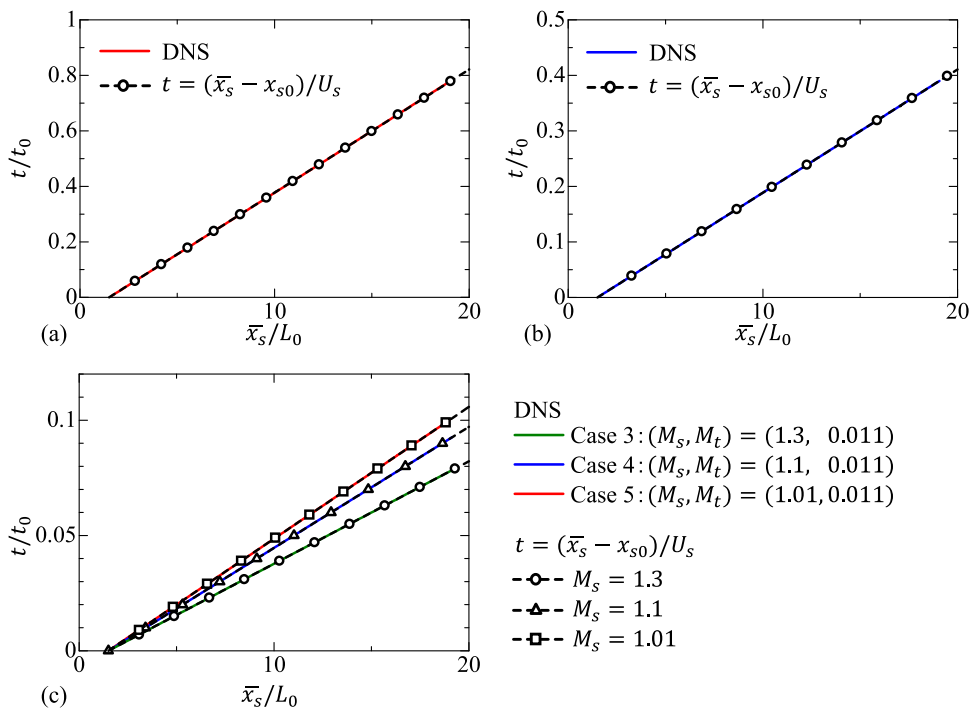


FIG. 5. Relation between mean shock wave positions \bar{x}_s and time t : (a) case 1 ($M_t = 0.13$), (b) case 2 ($M_t = 0.063$), and (c) cases 3, 4, and 5 ($M_t = 0.011$).

Figure 5 shows the relation between the mean shock wave position \bar{x}_s and time t , which are normalized by the reference length and time scales (L_0 and $t_0 = L_0/u_0$) of the simulations; t_0 is the time scale of turbulence, which depends on M_t . The non-dimensional plots of \bar{x}_s/L_0 and t/t_0 are different even for the same shock Mach number in cases 1 and 2 because M_t is different in these cases. The figure also shows a linear relationship $\bar{x}_s = U_s t + x_{s0}$ with a constant propagation velocity of the shock wave, U_s . This is valid if U_s does not change with time from the initial propagation velocity that is determined solely by the initial M_s and mean temperature in front of the shock wave. The mean position of the shock wave is well-predicted by $\bar{x}_s = U_s t + x_{s0}$ for all cases, and the mean propagation velocity hardly changes from the initial condition even when the shock wave propagates in turbulence.

We evaluate shock wave deformation as fluctuations in the shock wave position $x'_s(y, z; t) = x_s(y, z; t) - \bar{x}_s(t)$. Figures 6(a) and 6(b) show the rms values of x'_s , which is denoted by $x'_{s,rms}$, normalized by η , plotted against the mean shock wave position \bar{x}_s/L_0 . Here, η is taken in turbulence before the interaction with the shock wave. Cases 1–3 with $M_s = 1.3$ are compared in Fig. 6(a), whereas cases 3–5 with $M_t = 0.011$ are compared in Fig. 6(b). The shock wave at $\bar{x}_s/L_0 \geq 2.5$ is located within the turbulent region. $x'_{s,rms}$ starts increasing once the shock wave enters the turbulent region at $\bar{x}_s \approx 2.5L_0$ in the all cases. After the shock wave propagates for sufficiently long time, $x'_{s,rms}$ only weakly depends on the propagation distance (time) for $\bar{x}_s \geq 12L_0$. Here, $x'_{s,rms}$, except case 5, slightly decreases after a peak and then becomes almost independent of time. For case 5, with the smallest shock Mach number, $x'_{s,rms}$ tends to slowly increase with time until the end of the simulation; however,

the increase rate for $\bar{x}_s \geq 15L_0$ becomes very small. Normalized values of $x'_{s,rms}/\eta$ in the steady state depend on the shock and turbulent Mach numbers. The results for cases 1–3 with $M_s = 1.3$ suggest that $x'_{s,rms}$ increases with the turbulent Mach number. For cases 3–5 with $M_t = 0.011$, $x'_{s,rms}$ decreases with the shock Mach number. In all cases, $x'_{s,rms}$ tends to be steady in late time, and this steady behavior of $x'_{s,rms}$ might be explained by the stability of the shock wave surface against small deformation.⁶³ The statistical convergence and spatial resolution effects are mentioned in the Appendix. Figure 6(c) plots $x'_{s,rms}/\eta$ against interaction time t_i/t_0 , which is defined as the time over which the shock wave propagates in the turbulent region $t_i = (\bar{x}_s - 2.5L_0)/U_s$. The relation between $x'_{s,rms}/\eta$ and t_i/t_0 confirms that the time required for the shock wave to be statistically steady is different in each case. However, the initial non-dimensional growth rate of $x'_{s,rms}/\eta$ is similar in all cases.

Hereafter, the time average is used for improving statistical convergence as $x'_{s,rms}$ tends to be independent of time after the shock wave propagates for a long period. The average is taken over a time period for which the mean shock wave position \bar{x}_s is located between $13L_0$ and $19L_0$. Figure 7(a) shows a probability density function (PDF) of x'_s normalized by $x'_{s,rms}$, which agrees well with the Gaussian function in all cases. Previous experimental and numerical studies also found that the Gaussian function is a good approximation of the PDF of various quantities related to a shock wave propagating in turbulence, e.g., fluctuations in pressure and density jumps across the shock wave.^{24,25,31,33} These previous experiments observed the Gaussian PDF of pressure-jump fluctuations for a weak spherical shock wave; the curvature effects of the shock surface can be negligible in the fluctuations in some shock wave properties. One-dimensional

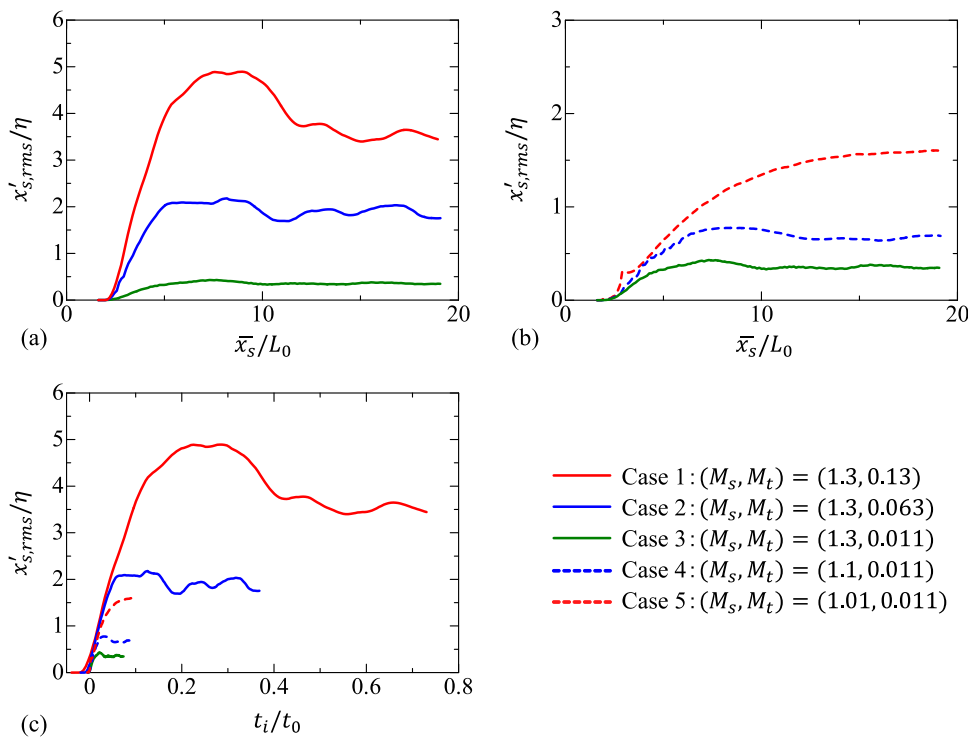


FIG. 6. Rms fluctuations in shock wave positions, $x'_{s,rms}$, plotted against [(a) and (b)] the mean position \bar{x}_s/L_0 and (c) the interaction time t_i/t_0 . Here, $x'_{s,rms}$ is normalized by the Kolmogorov scale η in turbulence at the initial state. (a) Turbulent Mach number dependence for $M_s = 1.3$ (cases 1–3) and (b) shock Mach number dependence for $M_t = 0.011$ (cases 3–5).

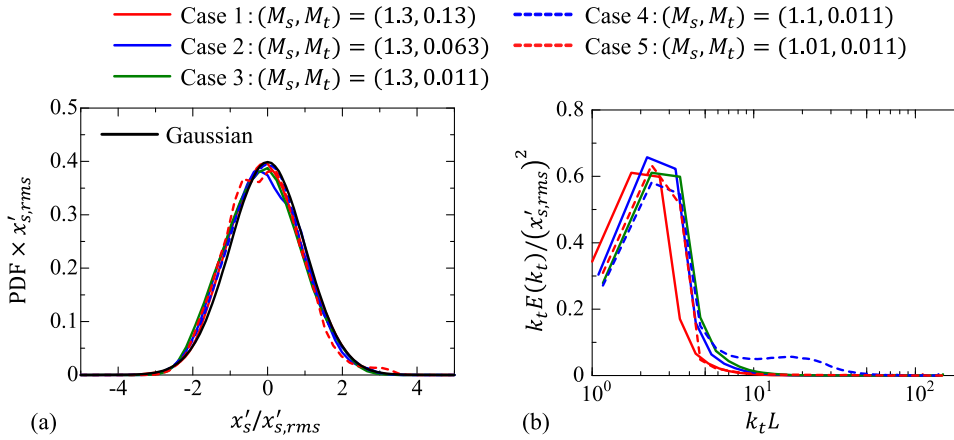


FIG. 7. (a) Probability density functions (PDFs) of x'_s normalized by $x'_{s,rms}$. (b) Energy spectra of x'_s , $E(k_t)$, in an area-preserving form, where k_t is a wavenumber in the transverse direction of the shock wave. Gray lines are obtained via two independent sets of five simulations of case 1.

Fourier transform in the y or z direction is applied to $x_s(y, z; t)$ to calculate the energy spectrum E . As x_s is statistically homogeneous and isotropic on a y - z plane, the spectrum of x_s is expressed as a function of the transverse wavenumber k_t , where the transverse direction is perpendicular to the x direction. Figure 7(b) shows the spectra of x'_s in an area-preserving form, $k_t E(k_t)$, where a visible area under the line represents contribution to $(x'_{s,rms})^2$. Here, k_t is normalized by the integral length scale L of turbulence. $k_t E$ becomes large for $k_t L \leq 6$, and fluctuations in x_s are dominated by large scales. These energy spectra are similar to pressure-jump spectra calculated using Fourier transform in the shock-transverse direction.²⁷ Dominant contribution of large scales to fluctuations in shock wave characteristics indicates the importance of large-scale motions in the turbulent effects on the shock wave.

All simulations are conducted with Re_λ in the range of 60–70, and the differences between each case should be attributed to M_t and M_s . The shock wave–turbulence interaction has been studied in relation to $M_t/(M_s - 1)$ and $M_t^2/(M_s^2 - 1)$ in previous studies.^{6,24,25,27,31,64} Figure 8 plots $x'_{s,rms}/\eta$ against $M_t/(M_s - 1)$ or $M_t^2/(M_s^2 - 1)$, where $x'_{s,rms}$ is evaluated for the shock wave with $13L_0 \leq \bar{x}_s \leq 19L_0$. All

cases have $\eta/L_0 \approx 0.012$, and $x'_{s,rms}$ is divided by an almost constant value. Therefore, Figs. 8(a) and 8(b) are used for assessing the relation between $x'_{s,rms}$ and $M_t/(M_s - 1)$ or $M_t^2/(M_s^2 - 1)$ but not for assessing the dependence on η . Figure 6 shows that $x'_{s,rms}/\eta$ increases with M_t and decreases with M_s , whereas both functions, $M_t/(M_s - 1)$ and $M_t^2/(M_s^2 - 1)$, similarly change with M_s and M_t . However, $x'_{s,rms}/\eta$, as shown in Fig. 8, is better expressed as a function of $M_t^2/(M_s^2 - 1)$ than $M_t/(M_s - 1)$, and $x'_{s,rms}/\eta$ exhibits a power law behavior of $M_t^2/(M_s^2 - 1)$. Applying the least squares method yields the following relation:

$$x'_{s,rms}/\eta \sim \left(\frac{M_t^2}{M_s^2 - 1} \right)^{0.46}. \quad (14)$$

For this relation, $x'_{s,rms}$ is almost proportional to M_t for fixed M_s , as also confirmed in Fig. 8(a). Experimental and numerical data of the shock wave–turbulence interaction^{25,27,29,31} compiled in Ref. 31 also show that rms fluctuations in the pressure jumps of shock waves, $P'_{s,rms}$, divided by the mean pressure jump, \bar{P}_s , change with $P'_{s,rms}/\bar{P}_s \sim [M_t^2/(M_s^2 - 1)]^{0.49}$, whose exponent is close to Eq. (14).

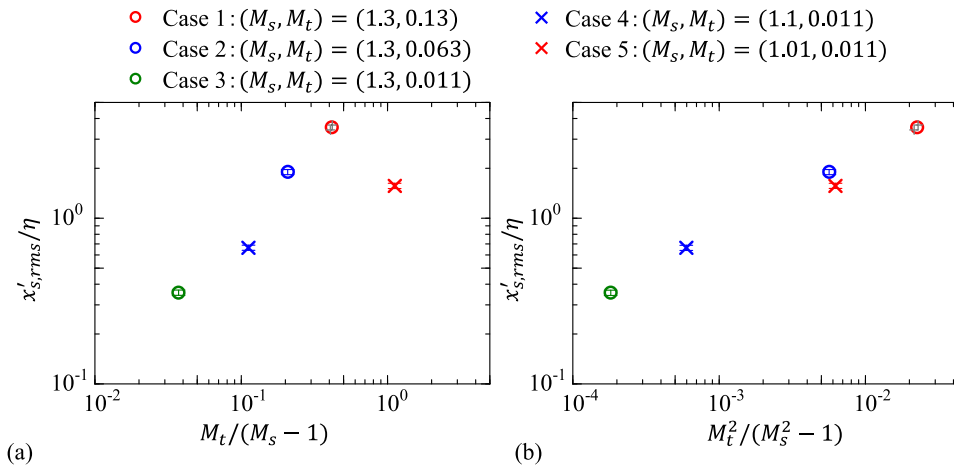


FIG. 8. $x'_{s,rms}/\eta$ plotted against (a) $M_t/(M_s - 1)$ and (b) $M_t^2/(M_s^2 - 1)$. The solid line in (b) represents a power law obtained using the least squares method. Gray “+” symbols are obtained by two independent sets of five simulations of case 1. Error bars for cases 2–5 represent 3.3% of the fractional error in $x'_{s,rms}$.

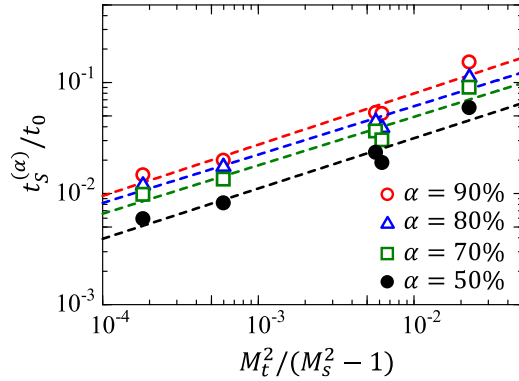


FIG. 9. Time scales $t_s^{(\alpha)}$ of the growth of $x'_{s,rms}$ divided by t_0 , plotted against $M_t^2/(M_s^2 - 1)$. Broken lines represent $t_s^{(\alpha)}/t_0 = A[M_t^2/(M_s^2 - 1)]^n$ obtained using the least squares method.

A simplified argument of shock wave deformation,³¹ which successfully predicts a power law behavior $P'_{s,rms}/\bar{P}_s \sim [M_t^2/(M_s^2 - 1)]^{0.5}$, shows that shock wave deformation can cause pressure-jump fluctuations. Similar scaling exponents of rms fluctuations in the pressure jump and shock wave position imply that shock wave deformation is an appropriate measure of fluctuations in the shock wave strength, which determines the local pressure jump across the shock wave. The power law of $P'_{s,rms}$ in Ref. 31 was obtained from experimental and numerical data for both normal and spherical shock waves, and these shock waves have a very similar dependence on $P'_{s,rms}$ on $[M_t^2/(M_s^2 - 1)]$. Considering the relation between shock wave deformation and pressure jump fluctuations,³¹ the scaling law of $x'_{s,rms}$ is also expected to be valid in spherical shock waves with a large curvature.

In Fig. 6, $x'_{s,rms}/\eta$ gradually increases as the shock wave propagates in turbulence. We define $x_s^{(\alpha)}$ as the shock wave position at which $x'_{s,rms}$ reaches $\alpha\%$ of the maximum value of $x'_{s,rms}$. An order of the time scale for the growth of $x'_{s,rms}$ can be roughly estimated as $t_s^{(\alpha)} = (x_s^{(\alpha)} - x_{s0})/U_s$, where the shock wave propagates in

turbulence for a time interval of $t_s^{(\alpha)}$ until $x'_{s,rms}$ reaches $\alpha\%$ of its maximum value. Although the present definition of $t_s^{(\alpha)}$ does not provide an exact time for the shock wave to be in a statistically steady state, $t_s^{(\alpha)}$ is still useful to observe the dependence of the time scale of shock wave deformation on M_s and M_t . Figure 9 shows the relations between $t_s^{(\alpha)}/t_0$ and $M_t^2/(M_s^2 - 1)$ for $50\% \leq \alpha \leq 90\%$ for all cases. Although $t_s^{(\alpha)}/t_0$ depends on α because of the definition, it generally increases with $M_t^2/(M_s^2 - 1)$. This trend is possibly explained by a time scale of deformation due to velocity fluctuations, which can be estimated as $t_s = x'_{s,rms}/u_0$. In the DNS used herein, L_0/η is almost constant because the Reynolds number is similar in all cases. The power law of $x'_{s,rms}$, Eq. (14), can be read as $x'_{s,rms} \sim L_0[M_t^2/(M_s^2 - 1)]^{0.46}$. Then, the following scaling law of t_s normalized by the integral time scale $t_0 = L_0/u_0$ is obtained from an empirical relation of Eq. (14):

$$t_s/t_0 \sim \left(\frac{M_t^2}{M_s^2 - 1} \right)^{0.46}. \quad (15)$$

This relation holds for the present DNS data shown in Fig. 9: the least squares method yields exponents of the power law, written as $t_s^{(\alpha)}/t_0 = A[M_t^2/(M_s^2 - 1)]^n$, where $n = 0.46, 0.44, 0.44$, and 0.45 are obtained for $\alpha = 90\%, 80\%, 70\%$, and 50% , respectively. These values are close to 0.46, and Eq. (15) is a fairly good approximation of the deformation time scale at the initial stage of the interaction.

C. Relation between local shock wave characteristics and the shock wave position

We investigate local shock wave characteristics in relation to shock wave deformation, where time instances with $13L_0 \leq \bar{x}_s \leq 19L_0$ are used for calculating the statistics. Dilatation $\theta \equiv \nabla \cdot \mathbf{u}$ evaluated at the shock wave position x_s is denoted by $\theta_s(y, z; t) = \theta(x_s, y, z; t)$. Figure 10 shows a joint PDF between x'_s and $\theta'_s = \theta_s - \bar{\theta}_s$ in cases 1 and 5. These quantities are positively correlated: the dilatation tends to be small when the shock wave is located behind the mean shock wave position and vice versa. With Eq. (1), the dilatation can also be written as $\theta = -(1/\rho)(D\rho/Dt)$. The positive correlation between x'_s and θ'_s suggests that the shock wave with $x'_s < 0$ tends to have a stronger compression with a higher local

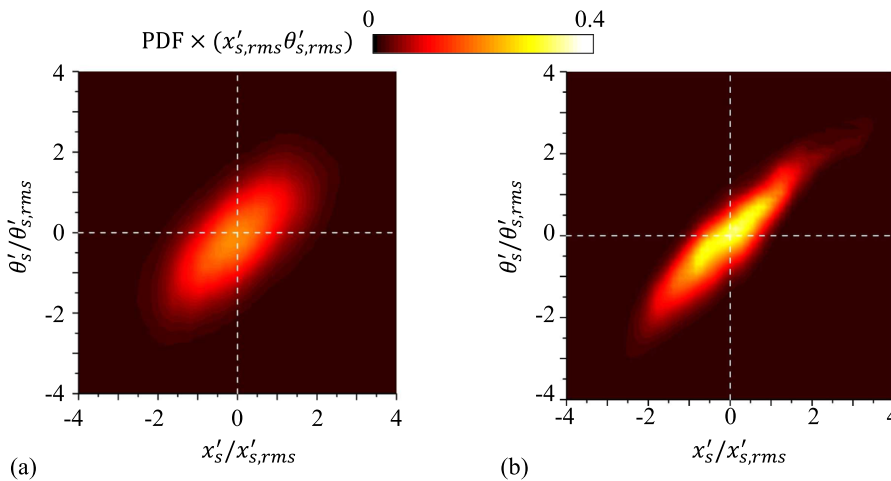


FIG. 10. Joint PDF between x'_s and θ'_s in (a) case 1 and (b) case 5.

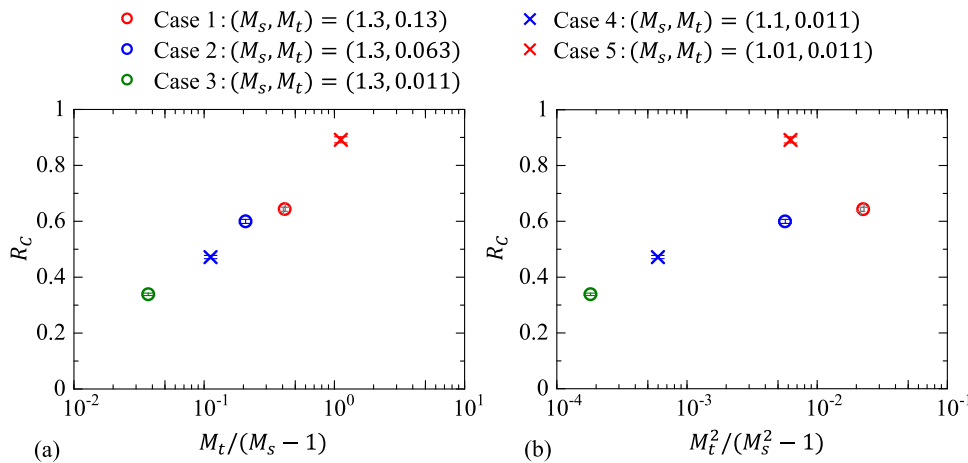


FIG. 11. Correlation coefficients R_C between x'_s and θ'_s plotted against (a) $M_t/(M_s - 1)$ and (b) $M_t^2/(M_s^2 - 1)$. Gray “+” symbols are obtained by two independent sets of five simulations of case 1. Error bars for cases 2–5 represent 1.2% of the fractional error in R_C .

shock Mach number. The correlation suggests that an area of the shock wave behind the mean shock wave position has a large propagation velocity, and x'_s approaches zero. Similarly, a shock wave area with $x'_s > 0$ has a smaller propagation velocity than average, and positive x'_s tends to decrease to 0. Stability of the shock surface against turbulence is explained by these relations between shock wave deformation and the local shock Mach number. The correlation between x'_s and θ'_s can be better explained by the relation between the curvature of the shock wave and the local strength of the shock wave, as also explained by Larsson *et al.*²⁵ The focusing effect on a concave region amplifies the local shock Mach number,³⁴ and the concave region is most likely to have a negative x'_s . A convex shape with the defocusing effect that weakens the shock wave is also likely to appear with $x'_s > 0$. These relations of the shock surface geometry result in a positive correlation between x'_s and θ'_s .

The correlation coefficient is calculated between x'_s and θ'_s . Figure 11 plots the correlation coefficient $R_C = x'_s \theta'_s / (x'_{s,rms} \theta'_{s,rms})$ against $M_t/(M_s - 1)$ or $M_t^2/(M_s^2 - 1)$. The Appendix also discusses the influences of statistical convergence on R_C . The maximum and minimum values of R_C are observed in cases 5 and 3, respectively. In cases 1–3, the correlation becomes weaker as the turbulent Mach number decreases from case 1 to case 3. Conversely, the correlation in cases 3–5 is stronger for a smaller shock Mach number. R_C increases with $M_t/(M_s - 1)$ in Fig. 11(a), whereas R_C plotted against $M_t^2/(M_s^2 - 1)$ has more scatters. Unlike $x'_{s,rms}$, the correlation between the shock wave position and dilatation is better characterized by $M_t/(M_s - 1)$ than $M_t^2/(M_s^2 - 1)$. Spatiotemporal correlation between a shock wave and turbulence has been investigated in numerical simulations and wind tunnel experiments of the shock wave–turbulence interaction.^{27,30} These studies confirmed that there is a time lag for the interaction to alter the pressure jump of the shock wave. A simple model of shock wave deformation implies that the effects of turbulence on the pressure jump, i.e., the local shock Mach number and dilatation, emerge more rapidly for a smaller M_t or a larger M_s .³⁰ Dilatation fluctuations at x_s are caused by turbulence that has interacted with the shock wave before it reaches x_s . For a small M_t or a large M_s , the interaction that occurs until the shock wave reaches x_s rapidly affects the dilatation of the shock wave, and the correlation between x'_s and θ'_s can be

weakened. Therefore, these time-lag effects of the shock wave response to turbulence can be a possible reason for R_C to increase with $M_t/(M_s - 1)$.

We investigate the mean pressure jump across the shock wave using averages conditioned on the local distance from the shock wave in the x direction, which is defined as $\Delta x_s = x - x_s$. An average conditioned on Δx_s is denoted by $\langle f | \Delta x_s \rangle$, which is calculated using the time average, averages in the y and z directions, and ensemble averages of five simulations. Here, the time average is taken for a time period with $13L_0 \leq \bar{x}_s \leq 19L_0$. A normalized mean pressure jump is defined as $\Delta P = (\langle P | \Delta x_s \rangle - P_F) / (P_B - P_F)$, where P_B and P_F are the initial mean pressures behind and in front of the shock wave, respectively. With this definition, ΔP changes from 0 to 1 across the shock wave. Dilatation within the shock wave represents the strength of the compression by the shock wave; therefore, x'_s should also be correlated with the pressure jump across the shock wave. The relation between x'_s and the pressure jump is assessed with the ΔP calculated separately for the shock wave positions with $x'_s > 0$ and $x'_s < 0$, where the ΔP calculated for $x'_s > 0$ and $x'_s < 0$ are denoted by $(\Delta P)_{x'_s}^+$ and $(\Delta P)_{x'_s}^-$, respectively. Figure 12 compares ΔP , $(\Delta P)_{x'_s}^+$, and $(\Delta P)_{x'_s}^-$ in case 1. As expected from the above discussion, one

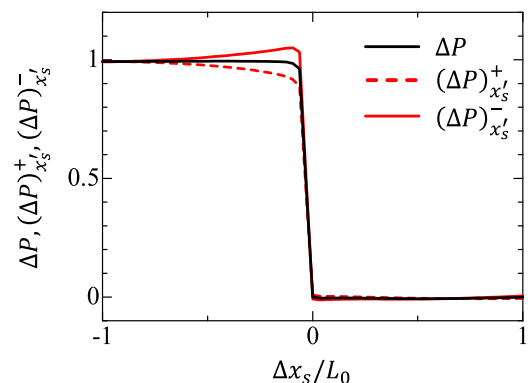


FIG. 12. Mean pressure jumps ΔP , $(\Delta P)_{x'_s}^+$, and $(\Delta P)_{x'_s}^-$ in case 1. $(\Delta P)_{x'_s}^+$ and $(\Delta P)_{x'_s}^-$ are calculated for $x'_s > 0$ and $x'_s < 0$, respectively.

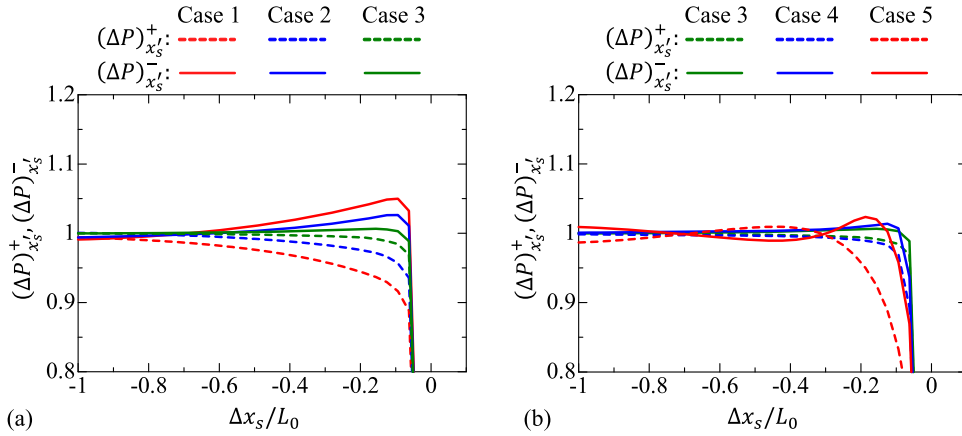


FIG. 13. Mean pressure jumps obtained separately for $x'_s > 0$ and $x'_s < 0$, which are denoted by $(\Delta P)_{x'_s}^+$ and $(\Delta P)_{x'_s}^-$, respectively: (a) cases 1–3 and (b) cases 3–5.

can find a large pressure jump for $x'_s < 0$ and a small pressure jump for $x'_s > 0$. Figures 13(a) and 13(b) show $(\Delta P)_{x'_s}^+$ and $(\Delta P)_{x'_s}^-$ in all cases, which confirm similar dependence of the mean pressure jump on x'_s . The difference between $(\Delta P)_{x'_s}^+$ and $(\Delta P)_{x'_s}^-$ becomes large as M_t increases, as shown in Fig. 13(a), and as M_s decreases, as shown in Fig. 13(b).

Since the pressure jump is amplified when the shock wave is located behind the mean position, $(\Delta P)_{x'_s}^-$ attains a peak, as shown in Fig. 13. The pressure-jump difference between $x'_s < 0$ and $x'_s > 0$ is evaluated as $(\Delta P)_{x'_s}^- - (\Delta P)_{x'_s}^+$ at the peak location of $(\Delta P)_{x'_s}^-$. As the shock wave tends to be strong and weak for $x'_s < 0$ and $x'_s > 0$, respectively, $(\Delta P)_{x'_s}^- - (\Delta P)_{x'_s}^+$ is a measure of the pressure-jump fluctuations normalized by the mean pressure-jump. Figure 14(a) plots $(\Delta P)_{x'_s}^- - (\Delta P)_{x'_s}^+$ against $x'_{s,rms}/\eta$. $(\Delta P)_{x'_s}^- - (\Delta P)_{x'_s}^+$ increases with $x'_{s,rms}$, and the pressure-jump fluctuations become stronger with shock wave deformation. Figure 14(b) shows $(\Delta P)_{x'_s}^- - (\Delta P)_{x'_s}^+$ plotted against $M_t^2/(M_s^2 - 1)$. $(\Delta P)_{x'_s}^- - (\Delta P)_{x'_s}^+$ seems to be well expressed as a function of $M_t^2/(M_s^2 - 1)$. This result is consistent with experimental studies,³¹ which also confirmed that the rms fluctuation in the pressure jump divided by the mean pressure jump increases with a power law of $M_t^2/(M_s^2 - 1)$.

In experiments assessing the interaction between a spherical shock wave and a turbulent jet,²⁸ the relation between the pressure jump of the shock wave and the shock wave geometry has been examined using schlieren images and pressure measurements. They showed that a shock wave with a concave shape in the propagation direction tends to have a large pressure jump. The concave shape is formed when the shock wave position is locally behind the mean shock wave position, and this experimental result is consistent with the numerical simulations conducted in this study. In addition, a positive correlation was observed between the shock wave position and the density jump obtained via DNS.²⁵ Previous numerical simulations and experiments confirm that velocity fluctuations in turbulence in the shock normal direction are also correlated with fluctuations in the pressure jump.^{27,30,33} The fact that both the velocity in turbulence and local shock wave position are correlated with the pressure jump suggests that shock wave deformation is mainly caused by velocity fluctuations in turbulence. The velocity of the shock wave movement is represented as the sum of the shock propagation velocity and flow velocity at which the shock wave is located. The turbulent velocity field results in a non-uniform shock movement velocity. For example, velocity fluctuations in the opposite direction of propagation decrease the shock

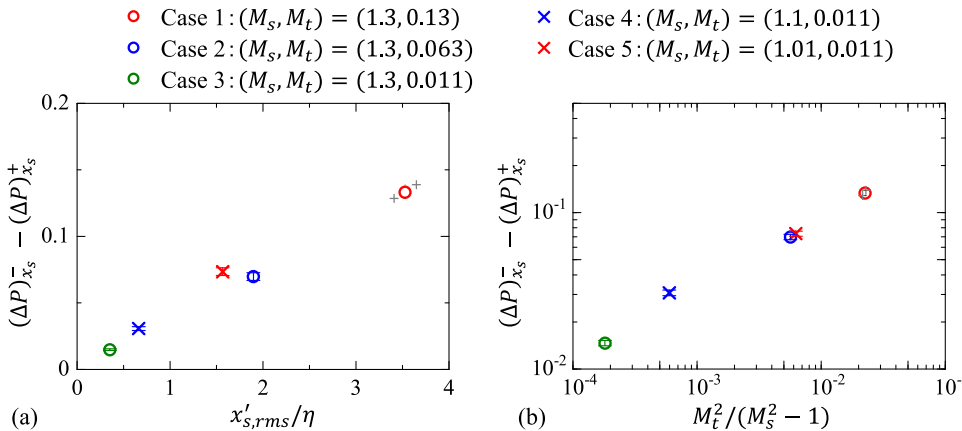


FIG. 14. Difference between mean pressure jumps $(\Delta P)_{x'_s}^+$ and $(\Delta P)_{x'_s}^-$, which are calculated for $x'_s > 0$ and $x'_s < 0$, respectively. $(\Delta P)_{x'_s}^- - (\Delta P)_{x'_s}^+$ is evaluated at the location where $(\Delta P)_{x'_s}^-$ reaches a peak. The results are presented against (a) $x'_{s,rms}/\eta$ and (b) $M_t^2/(M_s^2 - 1)$. Gray + symbols are obtained by two independent sets of five simulations of case 1. Error bars represent 3.9% of the fractional error in $(\Delta P)_{x'_s}^- - (\Delta P)_{x'_s}^+$.

movement velocity, resulting in a negative x'_s . Conversely, a positive x'_s is obtained via velocity fluctuations in the propagation direction. This relation between x'_s and velocity fluctuations can explain the correlation among x'_s , velocity, and jumps of pressure and density or dilatation observed in experiments and numerical simulations. Temperature fluctuations that affect the speed of sound can also cause shock wave deformation. This effect may be significant at very high turbulent Mach numbers, which are not considered in the numerical simulations conducted in this study.

In previous studies, both $M_t/(M_s - 1)$ and $M_t^2/(M_s^2 - 1)$ have been used for characterizing the shock wave–turbulence interaction. Statistics in some papers are better organized by $M_t/(M_s - 1)$ (e.g., the broken regime of the interaction²⁵), while other papers claim that their statistics are well-represented as functions of $M_t^2/(M_s^2 - 1)$ (e.g., variance of pressure jumps³⁰). The characteristics of turbulence are often very different among these papers. For example, isotropic turbulence considered in numerical simulations may have different thermodynamic properties that depend on forcing schemes even for the same turbulent Mach number. Therefore, previous studies could not have concluded if $M_t/(M_s - 1)$, $M_t^2/(M_s^2 - 1)$, or neither of them is the dominant parameter of the shock wave–turbulence interaction. The simulations in this study revealed that $x'_{s,rms}$ and $(\Delta P)_{x'_s}^- - (\Delta P)_{x'_s}^+$ are well-expressed as functions of $M_t^2/(M_s^2 - 1)$, whereas the correlation between the shock wave position and dilatation is well-organized with $M_t/(M_s - 1)$. The present results suggest that whether the interaction is better characterized by $M_t/(M_s - 1)$ or $M_t^2/(M_s^2 - 1)$ depends on quantities of interest.

IV. CONCLUSION

We performed DNS for a normal shock wave that propagates from a flow at rest toward a local turbulent region, which is generated using homogeneous isotropic turbulence. Here, the shock Mach number M_s and turbulent Mach number M_t range between 1.01 and 1.3 and between 0.011 and 0.13, respectively, whereas the turbulent Reynolds number is 60–70 in all simulations. Most previous numerical studies on the shock wave–turbulence interaction have investigated a statistically steady state of the interaction, which is achieved after the shock wave has propagated for sufficiently long time. In this study, the flow setup of the simulation enabled us to investigate the initial transition stage of the interaction, where the effects of the interaction gradually emerge on the shock wave. The local shock wave position was identified through a local peak of the pressure gradient in the propagation direction. This position enabled us to investigate the statistical properties of shock wave deformation.

The following important characteristics of shock wave deformation were found in the initial stage of the interaction.

- The shock wave gradually deforms once it enters the turbulent region. Here, the rms fluctuation in the shock wave position, $x'_{s,rms}$, increases with time, and it reaches a steady state after the shock wave propagates in turbulence for a long time interval.
- The time scale of the initial growth of shock wave deformation is well-characterized by the integral time scale t_0 of turbulence.

In the statistically steady state of the interaction, the DNS performed in this study revealed the following characteristics of the shock wave.

- $x'_{s,rms}$ increases with a power law of $M_t^2/(M_s^2 - 1)$, where the exponent of the power law is 0.46 in the DNS used herein. This scaling exponent is similar to that obtained for the rms pressure-jump fluctuation divided by the mean pressure jump,³¹ which also increases with a power law of $M_t^2/(M_s^2 - 1)$.
- The PDF of fluctuations in the shock wave position was approximated well by the Gaussian function.
- The fluctuations in the shock wave position are dominated by large-scale fluctuations whose length scale is similar to the integral length scale of turbulence.

The scaling of $x'_{s,rms}$ and the time scale of the initial growth of shock wave deformation indicate that the time period of the initial transition stage is proportional to $t_0[M_t^2/(M_s^2 - 1)]^{0.46}$, which was indeed confirmed in the DNS used herein.

The effects of shock wave deformation on local shock wave properties were investigated using dilatation and pressure jumps of the shock wave. Dilatation, which represents the strength of compression, is correlated with the fluctuations in the shock wave position, where the correlation becomes stronger as $M_t/(M_s - 1)$ increases. The sign of the correlation indicates that the shock wave that has deformed backward tends to be strong and vice versa. The mean pressure jump across the shock wave was calculated based on whether the shock wave had deformed forward or backward. As expected from the correlation, an area with backward deformation tends to have a large pressure jump, whereas a smaller pressure jump appears for shock waves with forward deformation. The difference between the conditional mean pressure jump under these two conditions increases with the rms fluctuation in the shock wave position and is represented well as a function of $M_t^2/(M_s^2 - 1)$.

The present analysis is based on the statistics of turbulence and the shock wave. It is expected that future works will elucidate the role of turbulent structures in the shock wave–turbulence interaction for better understanding of the physical mechanism of the interaction that modulates the shock wave. This study considers a shock wave propagating in the local region of isotropic turbulence. In many practical problems, turbulent flows are anisotropic and inhomogeneous. The effects of the anisotropy of turbulence and inhomogeneity need to be further studied for better understanding of the shock–turbulence interaction.

ACKNOWLEDGMENTS

The authors acknowledge Professor A. Sasoh and Mr. G. Fukushima (Nagoya University) for stimulating discussion. Direct numerical simulations of homogeneous isotropic turbulence presented in this paper were performed using the high-performance computing system in the Japan Agency for Marine–Earth Science and Technology. This work was also supported by the “Collaborative Research Project on Computer Science with High-Performance Computing in Nagoya University” and by the JSPS KAKENHI, Grant Nos. 19J12973 and 18H01367.

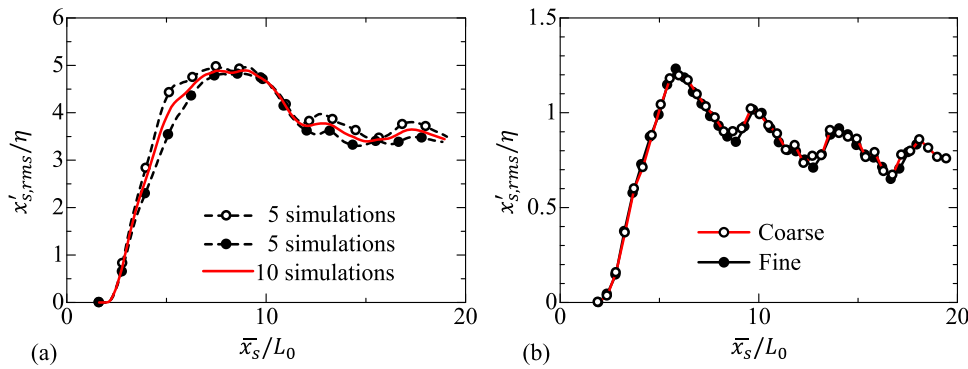


FIG. 15. (a) $x'_{s,rms}$ is calculated via two independent sets of five simulations of case 1, where $x'_{s,rms}$ obtained from the ten simulations is also shown for comparison. (b) $x'_{s,rms}$ obtained from simulations with different spatial resolutions, where the fine and coarse cases have $\Delta/\eta = 0.34$ and 1.3, respectively.

NOMENCLATURE

Δ	computational grid size
Δx_s	distance from the shock wave
γ	specific heat ratio
δ_{ij}	Kronecker delta
ε	dissipation rate of turbulent kinetic energy
η	Kolmogorov length scale
θ_s	dilatation at the shock wave position
κ	thermal conductivity
λ	Taylor microscale
μ	viscosity coefficient
ν	kinematic viscosity
ρ	density
τ_{ij}	shear stress tensor
a	speed of sound
e	total energy
\bar{f}	average of f
f'	fluctuations of f from average
f'_{rms}	root-mean-squared fluctuation of variable f
L	integral length scale
L_0	reference length scale used for normalization in DNS
L_x, L_y, L_z	computational domain size in each direction
M_s	shock Mach number
M_t	turbulent Mach number
N_x, N_y, N_z	number of grid points in each direction
P	pressure
R	gas constant
Re_λ	turbulent Reynolds number
T	temperature
t	time
t_0	reference time scale used for normalization in DNS
u, v, w	velocity components in x, y , and z directions
u_0	reference velocity scale used for normalization in DNS
u_i	velocity component in the i direction
U_s	shock wave propagation velocity
x, y, z	position
x_i	position in the i direction
x_s	shock wave position

APPENDIX: EFFECTS OF STATISTICAL CONVERGENCE AND THE SPATIAL RESOLUTION

The effects of the number of statistical samples are investigated for case 1, for which ten independent simulations are

conducted using different snapshots of homogeneous isotropic turbulence. These ten simulations are divided into two sets of five simulations, for which $x'_{s,rms}$ is separately calculated. Figure 15(a) shows $x'_{s,rms}$ calculated from each set or all simulations. Three lines of $x'_{s,rms}$ are very similar. At the end of the simulation, the difference in $x'_{s,rms}$ between two sets of five simulations is 0.11η , which is much smaller than $x'_{s,rms}$. Therefore, the number of the samples does not affect the discussion on $x'_{s,rms}$. The statistical convergence of R_C is also checked using two independent sets of five simulations used in Fig. 15(a), for which $R_C = 0.65$ and 0.64 are obtained. Therefore, the number of samples barely affects the results of R_C , which is presented in Fig. 11.

The effects of the spatial resolution on the analysis of $x'_{s,rms}$ are examined with additional simulations of the shock wave–turbulence interaction for $(M_s, M_t, Re_\lambda) = (1.3, 0.13, 20)$, whose Re_λ is smaller than that in the other simulations. Simulations with a low Re_λ are performed with two grid settings. One uses fine grids with $(N_x, N_y, N_z) = (2048, 256, 256)$, while another one uses coarse grids with $(N_x, N_y, N_z) = (512, 64, 64)$. For this Reynolds number, the grid sizes Δ/η are 0.34 and 1.3 for the fine and coarse grid settings, respectively. Here, the initial conditions are identical for the two simulations. Figure 15(b) shows $x'_{s,rms}$ obtained using the fine and coarse grids. $x'_{s,rms}$ is hardly affected by the spatial resolution, confirming that the grid size $\Delta/\eta \approx 1.4$ is small enough to investigate the statistics of x_s .

DATA AVAILABILITY

The data that support the findings of this study are available from the corresponding author upon reasonable request.

REFERENCES

- ¹M.-M. Mac Low and R. S. Klessen, “Control of star formation by supersonic turbulence,” *Rev. Mod. Phys.* **76**, 125 (2004).
- ²V. A. Thomas and R. J. Kares, “Drive asymmetry and the origin of turbulence in an ICF implosion,” *Phys. Rev. Lett.* **109**, 075004 (2012).
- ³D. J. Maglieri, “Some effects of airplane operations and the atmosphere on sonic-boom signatures,” *J. Acoust. Soc. Am.* **39**, S36–S42 (1966).
- ⁴C. Cerri, “The effects of sonic boom on the ecological environment,” *J. Navig.* **33**, 296–303 (1980).
- ⁵M. Kanamori, T. Takahashi, Y. Makino, Y. Naka, and H. Ishikawa, “Comparison of simulated sonic boom in stratified atmosphere with flight test measurements,” *AIAA J.* **56**, 2743–2755 (2018).
- ⁶S. Lee, S. K. Lele, and P. Moin, “Direct numerical simulation of isotropic turbulence interacting with a weak shock wave,” *J. Fluid Mech.* **251**, 533–562 (1993).

- ⁷S. Lee, S. K. Lele, and P. Moin, "Interaction of isotropic turbulence with shock waves: Effect of shock strength," *J. Fluid Mech.* **340**, 225–247 (1997).
- ⁸D. Livescu and J. Ryu, "Vorticity dynamics after the shock-turbulence interaction," *Shock Waves* **26**, 241–251 (2016).
- ⁹R. Boukharfane, Z. Bouali, and A. Mura, "Evolution of scalar and velocity dynamics in planar shock-turbulence interaction," *Shock Waves* **28**, 1117–1141 (2018).
- ¹⁰C. H. Chen and D. A. Donzis, "Shock-turbulence interactions at high turbulence intensities," *J. Fluid Mech.* **870**, 813–847 (2019).
- ¹¹Y. P. M. Sethuraman and K. Sinha, "Effect of turbulent Mach number on the thermodynamic fluctuations in canonical shock-turbulence interaction," *Comput. Fluids* **197**, 104354 (2020).
- ¹²J. Keller and W. Merzkirch, "Interaction of a normal shock wave with a compressible turbulent flow," *Exp. Fluids* **8**, 241–248 (1990).
- ¹³J. H. Agui, G. Briassulis, and Y. Andreopoulos, "Studies of interactions of a propagating shock wave with decaying grid turbulence: Velocity and vorticity fields," *J. Fluid Mech.* **524**, 143–195 (2005).
- ¹⁴T. Kitamura, K. Nagata, Y. Sakai, A. Sasoh, and Y. Ito, "Changes in divergence-free grid turbulence interacting with a weak spherical shock wave," *Phys. Fluids* **29**, 065114 (2017).
- ¹⁵H. S. Ribner, "Shock-turbulence interaction and the generation of noise," NACA Report No. 1233, 1954.
- ¹⁶H. S. Ribner, "Convection of a pattern of vorticity through a shock wave," NACA Report No. 1164, 1954.
- ¹⁷F. K. Moore, *Unsteady Oblique Interaction of a Shock Wave with a Plane Disturbance* (National Advisory Committee for Aeronautics, 1953), Vol. 1165.
- ¹⁸L. Jacquin, C. Cambon, and E. Blin, "Turbulence amplification by a shock wave and rapid distortion theory," *Phys. Fluids* **5**, 2539–2550 (1993).
- ¹⁹K. Mahesh, S. K. Lele, and P. Moin, "The response of anisotropic turbulence to rapid homogeneous one-dimensional compression," *Phys. Fluids* **6**, 1052–1062 (1994).
- ²⁰T. Kitamura, K. Nagata, Y. Sakai, A. Sasoh, and Y. Ito, "Rapid distortion theory analysis on the interaction between homogeneous turbulence and a planar shock wave," *J. Fluid Mech.* **802**, 108–146 (2016).
- ²¹Y. P. M. Sethuraman, K. Sinha, and J. Larsson, "Thermodynamic fluctuations in canonical shock-turbulence interaction: Effect of shock strength," *Theor. Comput. Fluid Dyn.* **32**, 629–654 (2018).
- ²²N. O. Braun, D. I. Pullin, and D. I. Meiron, "Large eddy simulation investigation of the canonical shock-turbulence interaction," *J. Fluid Mech.* **858**, 500–535 (2019).
- ²³Y. P. M. Sethuraman and K. Sinha, "Modeling of thermodynamic fluctuations in canonical shock-turbulence interaction," *AIAA J.* **58**, 3076–3089 (2020).
- ²⁴J. Larsson and S. K. Lele, "Direct numerical simulation of canonical shock/turbulence interaction," *Phys. Fluids* **21**, 126101 (2009).
- ²⁵J. Larsson, I. Bermejo-Moreno, and S. K. Lele, "Reynolds- and Mach-number effects in canonical shock-turbulence interaction," *J. Fluid Mech.* **717**, 293 (2013).
- ²⁶T. Tamba, G. Fukushima, M. Kayumi, A. Iwakawa, and A. Sasoh, "Experimental investigation of the interaction of a weak planar shock with grid turbulence in a counter-driver shock tube," *Phys. Rev. Fluids* **4**, 073401 (2019).
- ²⁷K. Tanaka, T. Watanabe, K. Nagata, A. Sasoh, Y. Sakai, and T. Hayase, "Amplification and attenuation of shock wave strength caused by homogeneous isotropic turbulence," *Phys. Fluids* **30**, 035105 (2018).
- ²⁸J.-H. Kim, A. Sasoh, and A. Matsuda, "Modulations of a weak shock wave through a turbulent slit jet," *Shock Waves* **20**, 339–345 (2010).
- ²⁹A. Sasoh, T. Harasaki, T. Kitamura, D. Takagi, S. Ito, A. Matsuda, K. Nagata, and Y. Sakai, "Statistical behavior of post-shock overpressure past grid turbulence," *Shock Waves* **24**, 489–500 (2014).
- ³⁰K. Inokuma, T. Watanabe, K. Nagata, A. Sasoh, and Y. Sakai, "Finite response time of shock wave modulation by turbulence," *Phys. Fluids* **29**, 051701 (2017).
- ³¹K. Inokuma, T. Watanabe, K. Nagata, and Y. Sakai, "Statistics of overpressure fluctuations behind a weak shock wave interacting with turbulence," *Phys. Fluids* **31**, 085119 (2019).
- ³²K. Inokuma, T. Watanabe, K. Nagata, and Y. Sakai, "Statistical properties of spherical shock waves propagating through grid turbulence, turbulent cylinder wake, and laminar flow," *Phys. Scr.* **94**, 044004 (2019).
- ³³K. Aruga, K. Inokuma, T. Watanabe, K. Nagata, and Y. Sakai, "Experimental investigation of interactions between turbulent cylinder wake and spherical shock wave," *Phys. Fluids* **32**, 016101 (2020).
- ³⁴A. D. Pierce, "Statistical theory of atmospheric turbulence effects on sonic-boom rise times," *J. Acoust. Soc. Am.* **49**, 906–924 (1971).
- ³⁵F. Grasso and S. Pirozzoli, "Shock-wave-vortex interactions: Shock and vortex deformations, and sound production," *Theor. Comput. Fluid Dyn.* **13**, 421–456 (2000).
- ³⁶A. Rault, G. Chiavassa, and R. Donat, "Shock-vortex interactions at high Mach numbers," *J. Sci. Comput.* **19**, 347–371 (2003).
- ³⁷S. Zhang, Y.-T. Zhang, and C.-W. Shu, "Multistage interaction of a shock wave and a strong vortex," *Phys. Fluids* **17**, 116101 (2005).
- ³⁸S. B. Pope, *Turbulent Flows* (Cambridge University Press, 2000).
- ³⁹H. S. Ribner, P. J. Morris, and W. H. Chu, "Laboratory simulation of development of superbooms by atmospheric turbulence," *J. Acoust. Soc. Am.* **53**, 926–928 (1973).
- ⁴⁰A. Tsinober, *An Informal Conceptual Introduction to Turbulence* (Springer, 2009).
- ⁴¹K. Horiuti, "A classification method for vortex sheet and tube structures in turbulent flows," *Phys. Fluids* **13**, 3756–3774 (2001).
- ⁴²H. Mouri, A. Hori, and Y. Kawashima, "Laboratory experiments for intense vortical structures in turbulence velocity fields," *Phys. Fluids* **19**, 055101 (2007).
- ⁴³C. B. da Silva and J. C. F. Pereira, "Invariants of the velocity-gradient, rate-of-strain, and rate-of-rotation tensors across the turbulent/nonturbulent interface in jets," *Phys. Fluids* **20**, 055101 (2008).
- ⁴⁴R. Jahanbakhshi, N. S. Vaghefi, and C. K. Madnia, "Baroclinic vorticity generation near the turbulent/non-turbulent interface in a compressible shear layer," *Phys. Fluids* **27**, 105105 (2015).
- ⁴⁵B. M. Kirchner, G. S. Elliott, and J. C. Dutton, "Hairpin vortex structures in a supersonic, separated, longitudinal cylinder wake," *Phys. Fluids* **32**, 046103 (2020).
- ⁴⁶M. A. C. Teixeira and C. B. da Silva, "Turbulence dynamics near a turbulent/non-turbulent interface," *J. Fluid Mech.* **695**, 257–287 (2012).
- ⁴⁷R. R. Taveira and C. B. da Silva, "Characteristics of the viscous superlayer in shear free turbulence and in planar turbulent jets," *Phys. Fluids* **26**, 021702 (2014).
- ⁴⁸T. Watanabe, C. B. da Silva, K. Nagata, and Y. Sakai, "Geometrical aspects of turbulent/non-turbulent interfaces with and without mean shear," *Phys. Fluids* **29**, 085105 (2017).
- ⁴⁹T. Watanabe, C. B. da Silva, Y. Sakai, K. Nagata, and T. Hayase, "Lagrangian properties of the entrainment across turbulent/non-turbulent interface layers," *Phys. Fluids* **28**, 031701 (2016).
- ⁵⁰T. S. Silva and C. B. da Silva, "The behaviour of the scalar gradient across the turbulent/non-turbulent interface in jets," *Phys. Fluids* **29**, 085106 (2017).
- ⁵¹K. Takamure, Y. Ito, Y. Sakai, K. Iwano, and T. Hayase, "Momentum transport process in the quasi self-similar region of free shear mixing layer," *Phys. Fluids* **30**, 015109 (2018).
- ⁵²A. Jain and S. H. Kim, "On the non-equilibrium models for subfilter scalar variance in large eddy simulation of turbulent mixing and combustion," *Phys. Fluids* **31**, 025112 (2019).
- ⁵³J. Mi, M. Xu, and T. Zhou, "Reynolds number influence on statistical behaviors of turbulence in a circular free jet," *Phys. Fluids* **25**, 075101 (2013).
- ⁵⁴T. Watanabe, X. Zhang, and K. Nagata, "Direct numerical simulation of incompressible turbulent boundary layers and planar jets at high Reynolds numbers initialized with implicit large eddy simulation," *Comput. Fluids* **194**, 104314 (2019).
- ⁵⁵M. R. Petersen and D. Livescu, "Forcing for statistically stationary compressible isotropic turbulence," *Phys. Fluids* **22**, 116101 (2010).
- ⁵⁶X. Zhang, T. Watanabe, and K. Nagata, "Turbulent/nonturbulent interfaces in high-resolution direct numerical simulation of temporally evolving compressible turbulent boundary layers," *Phys. Rev. Fluids* **3**, 094605 (2018).

- ⁵⁷R. Nagata, T. Watanabe, and K. Nagata, "Turbulent/non-turbulent interfaces in temporally evolving compressible planar jets," *Phys. Fluids* **30**, 105109 (2018).
- ⁵⁸Y. Tai, T. Watanabe, and K. Nagata, "Modeling of molecular diffusion and thermal conduction with multi-particle interaction in compressible turbulence," *Phys. Fluids* **30**, 035108 (2018).
- ⁵⁹Z. Wang, Y. Lv, P. He, J. Zhou, and K. Cen, "Fully explicit implementation of direct numerical simulation for a transient near-field methane/air diffusion jet flame," *Comput. Fluids* **39**, 1381–1389 (2010).
- ⁶⁰C. A. Kennedy and M. H. Carpenter, "Several new numerical methods for compressible shear-layer simulations," *Appl. Numer. Math.* **14**, 397–433 (1994).
- ⁶¹D. Gefroh, E. Loth, C. Dutton, and E. Hafenrichter, "Aeroelastically deflecting flaps for shock/boundary-layer interaction control," *J. Fluids Struct.* **17**, 1001–1016 (2003).
- ⁶²F. Nicolas, V. Todoroff, A. Plyer, G. Le Besnerais, D. Donjat, F. Micheli, F. Champagnat, P. Cornic, and Y. Le Sant, "A direct approach for instantaneous 3D density field reconstruction from background-oriented schlieren (BOS) measurements," *Exp. Fluids* **57**, 13 (2016).
- ⁶³L. D. Landau and E. M. Lifshitz, *Course of Theoretical Physics: Fluid Mechanics* (Elsevier, 1987).
- ⁶⁴D. A. Donzis, "Shock structure in shock-turbulence interactions," *Phys. Fluids* **24**, 126101 (2012).